Title

Characterization of spatial statistics of distributed targets in SAR data

Permalink

https://escholarship.org/uc/item/3dm1d1h8

Journal

International Journal of Remote Sensing, 14(2)

ISSN
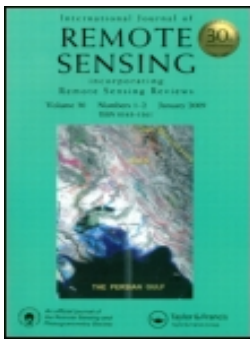
0143-1161

Authors

RIGNOT, E

KWOK, R

Publication Date

1993

DOI

10.1080/01431169308904341

Peer reviewed

Characterization of spatial statistics of distributed targets in SAR data

E. RIGNOT & R. KWOK

Characterization of spatial statistics of distributed targets in SAR data

E. RIGNOT and R. KWOK

Jet Propulsion Laboratory, California Institute of Technology,
4800 Oak Grove Drive, Pasadena, California 91109, U.S.A.

Abstract. A method for the analysis of spatial statistics in multifrequency polarimetric Synthetic Aperture Radar (SAR) data is presented. The objective is to extract the intrinsic variability of the target by removing the variability from other sources. Three sources which contribute to the spatial variability in the returned power from a distributed target are modelled, they are (1) image speckle, (2) system noise, and (3) the intrinsic spatial variability of the target or texture. Speckle and system noise are modelled based on an understanding of the physics of the SAR imaging and processing systems. Texture is modelled as a random variable which modulates the mean returned power from a distributed target. An image model which accounts for all three sources of variability is presented. The presence of texture is shown to increase the image variance-to-mean square ratio and to introduce deviations of the image autocovariance function from the expected SAR system response. Two textural parameters, the standard deviation of texture and its autocovariance coefficient, are examined. This statistical approach is illustrated using sea-ice SAR imagery acquired by the Jet Propulsion Laboratory three-frequency polarimetric airborne SAR. Textural modulation of the signal has been detected in the imagery. Results show that for different sea-ice types the spatial statistics seem to vary more across frequency than across polarization and the observed differences increase in magnitude with decreasing frequency. The results also suggest the potential of this approach for discrimination of various sea-ice types and open water in single frequency, single polarization SAR data. Correlation of the spatial statistics to field measurements will be important for the verification of these observations.

1. Introduction

The importance of characterizing the spatial variability of the backscattered radar signal from a remotely-sensed scene has been shown to be useful for the analysis of SAR data by many investigators (e.g., Laur 1989, Ulaby *et al.* 1986, Kouyate 1984, Lyden *et al.* 1984). Yet, more attention needs to be given to the effects of speckle noise, system noise, spatial resolution and incidence angle on the measurement of these statistics, especially if the goal is to develop an invariant measure which could be utilized with multi-temporal imagery.

Spatial statistics of natural targets are difficult to characterize in digital SAR imagery as the intrinsic spatial variability of the radar signal is strongly modulated by image speckle. Spatial statistics are also corrupted by system noise, especially in

the case of spaceborne systems where the signal-to-noise ratio is significantly lower than that for airborne systems. To obtain an absolute measure of the intrinsic spatial variability of the target it is necessary to remove the spatial modulation of the signal due to speckle and system noise. The measurements also need to be repeated at various incidence angles and at various spatial resolutions; this is because different scattering mechanisms may contribute to the observed backscatter at different incidence angles and different structural features may be revealed at different spatial resolutions and/or at various wavelengths.

In this context, techniques for quantitative analysis of spatial statistics based on post-processed SAR data, e.g., using a locally adaptive smoothing filter such as those of Lee (1981) or Frost *et al.* (1982) are sub-optimal since they modify the spatial resolution and in some cases the statistics of the data. Similarly, popular techniques originally designed for optical imagery such as they Grey Level Co-occurrence Matrix method (Haralick *et al.* 1973) are not well suited to the analysis of SAR imagery as they do not separate the intrinsic variability of the signal from the variability due to image speckle and system noise.

In this article, an approach is discussed which models three different sources which contribute to the spatial variability of the data: 1. image speckle, 2. system noise and 3. texture or intrinsic signal variability. The spatial statistics are extracted based on this model. Speckle and system noise are modelled based on the understanding of the physics of SAR imaging and processing. Texture is modelled as a random variable which modulates the mean returned power from a locally homogeneous area. The resulting composite image model is presented in §2. Based on this model, two textural parameters are estimated from the image data: 1. the variance of texture and 2. the autocovariance coefficient of texture. The sensitivity of these parameters to the SAR system impulse response, system noise, and the number of sample elements used for their estimation is discussed and the approach is applied to the analysis of spatial statistics of sea-ice in three-frequency polarimetric SAR data acquired by the NASA/JPL airborne SAR instrument.

2. Statistical image model and assumptions

In this approach, texture or the intrinsic spatial variability of the signal is modelled as a random modulation of the mean returned power from a distributed target. Let (i, j) denote the location of a pixel site in the image plane in pixel spacings, where i is an index in the range direction and j is an index in the azimuth direction. After reception, processing and detection of the radar signal, the power P of the radar return at pixel site (i, j) of region l is

$$P_{i,j,l} = [\langle I \rangle_l T_{i,j,l} + \langle n_i \rangle] S_{i,j} \tag{1}$$

where $\langle \ \rangle$ denotes the expected value, I is the backscattered power from the target, n is the additive system noise power, T is the texture random variable, and S is the image speckle random variable. T and S are independent normalized random variables (i.e., $\langle T \rangle = 1$; $\langle S \rangle = 1$), with stationary statistics, i.e., the mean is independent of the position and the autocorrelation function is translation invariant. The variance-to-mean square ratio of speckle ($\sigma_S^2/\langle S \rangle^2$) is equal to $1/N$ where N is the equivalent number of looks of the SAR data. The system noise power $\langle n_i \rangle$ is independent of the signal, I, texture, T, and speckle, S, but varies with slant-range. The speckle random variable $S_{i,j}$ does not depend on the region l of the image plane, and I has stationary statistics in each region l. A similar model was used in Ulaby *et*

al. (1986) although the contribution of system noise was not accounted for in this work.

Equation (1) defines a quasi-homogeneous image model as T modulates the mean backscattered power $\langle I \rangle_l$ of a locally homogeneous region indexed l. The model implicitly assumes that image speckle has the statistical characteristics of being multiplicative. In certain situations, this assumption may not be appropriate. The multiplicative model breaks down in the presence of dominant single scatterers (e.g., man-made structures) or when the autocorrelation function of the backscatter cross-section of the target does not vary smoothly from one resolution cell to the next (Madsen 1986).

The image model (1) also assumes that system noise is modulated by image speckle in the same manner as the signal. In effect, although system noise is composed of a suite of noise sources that occur at different stages of the SAR imaging and processing systems, its bandwidth in the processed data is usually limited by the SAR correlator bandwidth, and thus signal and system noise have nearly the same correlation properties.

Using (1) it is verified that the expected value of the detected power at pixel location (i,j) is the sum of the mean backscattered power and of the system noise power

$$\langle P_{i,j,l} \rangle = \langle I \rangle_l + \langle n_i \rangle. \tag{2}$$

2.1. *Variance of texture*

By computing the image variance using (1), the variance of texture σ_T^2 in region l is obtained as

$$\sigma_T^2 = \frac{N V_{mr} - 1}{(N+1)\left(\dfrac{\langle I \rangle_l}{<P>}\right)^2} \tag{3}$$

where V_{mr} is the image variance-to-mean square ratio, i.e., $V_{mr} = \sigma_P^2 / \langle P \rangle^2$, σ_P^2 is the image variance, and N is the equivalent number of looks. As previously defined, N is a first-order statistical characteristic of image speckle. It does not depend on the distribution of the backscatter cross-section of the imaged surface and is an intrinsic characteristic of the SAR imaging and processing systems. In single-look SAR intensity data, N is equal to one. In multi-look intensity data, N is computed using (Zelenka 1976)

$$N = \frac{\displaystyle\sum_{p,q=1}^{p,q=n} P_p P_q \rho_S(p,q)}{\left(\displaystyle\sum_{p=1}^{p=n} P_p\right)^2} \tag{4}$$

where n is the number of incoherently averaged samples used to produce the multi-look samples and ρ_S the autocovariance coefficient of speckle. When the n samples are independent, N equals n; but in most current SAR processors the selected samples are slightly correlated (due to sampling of the data) and the resulting equivalent number of looks N is less than n. An overestimated value of N results in an overestimated value of the variance of texture (3). To properly estimate N, ρ_S must be known. Its estimation is discussed in §3.3.

Equation (3) measures the increase in the image variance-to-mean square ratio compared to the speckle variance-to-mean square ratio, i.e., $1/N$. When the data are composed of pure speckle, V_{mr} is $1/N$, and σ_T^2 is zero. In the presence of texture, V_{mr} becomes larger than $1/N$, and the ratio increase is proportional to σ_T^2.

2.2. Autocovariance coefficient of texture

As the image field is assumed to be stationary in region l, the spatial correlation between two points separated by p pixels in range and q pixels in azimuth only depends on (p, q) and not on the absolute position of the points in the image plane. Using (1), the autocorrelation function of the image power P, denoted R_P, is

$$R_P(p, q) = (\langle I \rangle_l^2 \rho_T(p, q)\sigma_T^2 + \langle P \rangle^2)\left(1 + \frac{\rho_S(p, q)}{N}\right). \tag{5}$$

Assuming σ_T is non-zero, and using $R_P(p, q) = \rho_P(p, q)\sigma_P^2 + \langle P \rangle^2$, the autocovariance coefficient of texture is deduced as

$$\rho_T(p, q) = \frac{1}{\sigma_T^2}\left[\frac{\rho_P(p, q)V_{mr} - \frac{\rho_S(p, q)}{N}}{\left(1 + \frac{\rho_S(p, q)}{N}\right)\frac{\langle I \rangle_l^2}{\langle P \rangle^2}}\right]. \tag{6}$$

Using (3) and (4), (6) becomes

$$\rho_T(p, q) = \frac{N+1}{NV_{mr} - 1}\left[\frac{\rho_P(p, q)V_{mr} - \frac{\rho_S(p, q)}{N}}{1 + \frac{\rho_S(p, q)}{n}}\right]. \tag{7}$$

System noise does not appear in (7) as expected since its presence does not affect the correlation properties of the image field in our model. Equation (7) shows ρ_T measures the local broadening of the image autocovariance coefficient ρ_P from the expected autocovariance coefficient of speckle ρ_S. ρ_T varies between 0 and 1. The minimum value corresponds to a point where texture is highly decorrelated; the maximum value, $\rho_T = 1$, corresponds to a point with high correlation.

2.3. Other statistical models

The image model presented in (1) views texture as a random modulation of the backscatter cross-section (proportional to $\langle I \rangle_l$) of the target. An alternative description of the observed spatial variability of the signal can be obtained using correlated K-distributions. In that case, texture results from the spatial variability of the number of scatterers per resolution cell contributing to the total power return. The modelling approach is described in appendix D and the first and second order statistical characteristics of the signal are discussed and compared to those from our model.

3. Estimation of σ_T and ρ_T

The estimation accuracy of the two textural parameters given in (3) and (7) depends on the number of sample elements used for the computation of the local

image spatial statistics, and on the estimation accuracy of the autocovariance coefficient of speckle and of the system noise power level.

3.1. *Effect of window size*

Typically, a large number of samples is required to estimate the image variance and the image autocovariance of a SAR signal to a high level of confidence. In this section, the sensitivity of these parameters on the window size is discussed.

Using sampling distributions, Kendall and Stuart (1963) derived a general expression for computing the standard error for estimation of the V_{mr} ratio and the autocovariance coefficient ρ_P for a given window size based on the mth order statistics of the data. To examine the effect of window size on the standard error, an exponential distribution of the intensity is used for the one-look data and a Gamma distribution is used for N-look data. Although other distributions exist that model the data more accurately in some cases, the standard errors computed from these distributions will be assumed to be reasonably close (at least to first-order) to errors computed from more accurate distributions. In the limit of a very large equivalent number of looks, a Gaussian distribution of the intensity about its mean is used. Additional details are given in appendices A and B.

The percentage error of the V_{mr} ratio versus window size (assuming a square window) is plotted in figure 1 for one-look data and N-look (N infinite) data. The result indicates that in order to estimate V_{mr} with a high degree of confidence a window size larger than 20 pixel by 20 pixel elements is required.

The percentage error in the estimation of the image autocovariance coefficient versus window size is plotted in figure 2 for different values of ρ_P using one-look data. When ρ_P is large (i.e., larger than 0·6), a window size larger than 20 pixel by 20 pixel elements produces an estimation error less than 10 per cent. When ρ_P is small, the estimation noise is dominant and a large window size (i.e., larger than 50 by 50 elements) is necessary to improve the estimation. In digital SAR imagery, small values of ρ_P are commonly measured for a displacement of only a few pixels because of the strong modulation of the signal by image speckle which is weakly correlated due to sampling rates. Hence, only the first few values of the autocovariance coefficient can be estimated using a reasonable number of points. In the case of an infinite number of looks, the standard error is shown in figure 3. The error values are close to those given in figure 2, indicating that the gain in estimation accuracy of the autocovariance coefficient is small when images with large N are used instead of one-look images.

These standard errors in the determination of the image local statistics can be used to estimate the estimation errors of σ_T and ρ_T for a given window size. Equation (3) shows the error in σ_T^2 is proportional to the error in V_{mr} (assuming N is known). Equation (7) shows the error in ρ_T is large when V_{mr} is close to $1/N$ (i.e., little textural variability), otherwise is proportional to the error in ρ_P.

3.2. *Effect of system noise*

System noise is composed of a mixture of noise sources such as thermal noise from the receiver electronics, bit-error rate from transmission, quantization noise, side lobe noise, etc. It affects the statistical characteristics of the signal and thereby biases the measurement of textural features. As mentioned in §2, the autocovariance coefficient ρ_T is in general not affected by the presence of system noise. However, if

the contribution from system noise is ignored, σ_T will be estimated with a systematic error given by

$$\Delta\sigma_T = -1/(1 + SNR) \tag{8}$$

where *SNR* denotes the signal-to-noise ratio, i.e. $SNR = \langle I \rangle / \langle n \rangle$. The error is 100 per cent for a *SNR* performance of 0 dB. A 10 per cent error level is reached for a *SNR* performance less than 10 dB. In this paper, observations of textural variability of the signal are based on airborne SAR data from the NASA/JPL DC-8 SAR instrument where the system noise power level is low. The noise equivalent backscatter cross-section (the level at which the target backscattered power is equivalent to the noise power) is below −40 dB at *C*-, *L*-, and *P*-band frequencies between 30° and 60° incidence angle, i.e., more than 10 dB below the expected backscatter signatures of many sea-ice types at the currently observed frequencies, and therefore system noise can be neglected in the analysis. For comparison, the noise equivalent backscatter cross-section of the SAR data from the European First Earth Resources SAR Satellite E ERS-1 is expected to be only −18 dB. In that case the influence of system noise on the spatial statistical characteristics of the SAR signal must be considered during analysis of the data. This aspect is important as
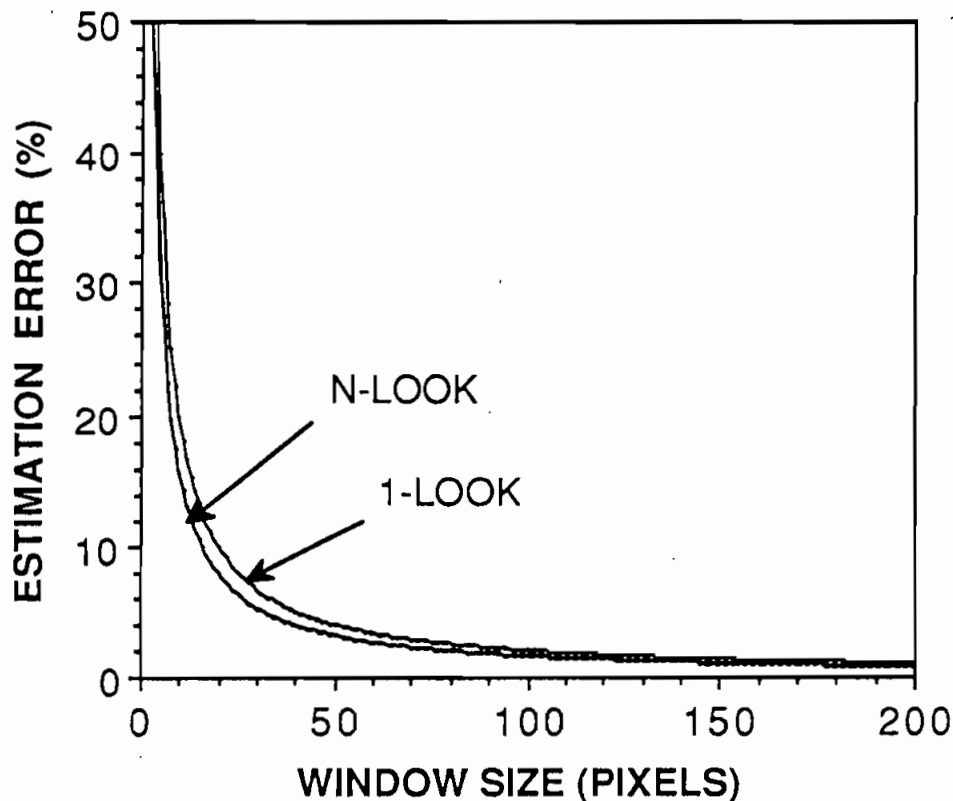

Figure 1. Estimation error of the image variance-to-mean square ratio $\sigma_P^2/\langle P \rangle^2$ for single (*l*-look) and multi-look (*N*-look) SAR data versus the size (in pixel samples) of a square window.
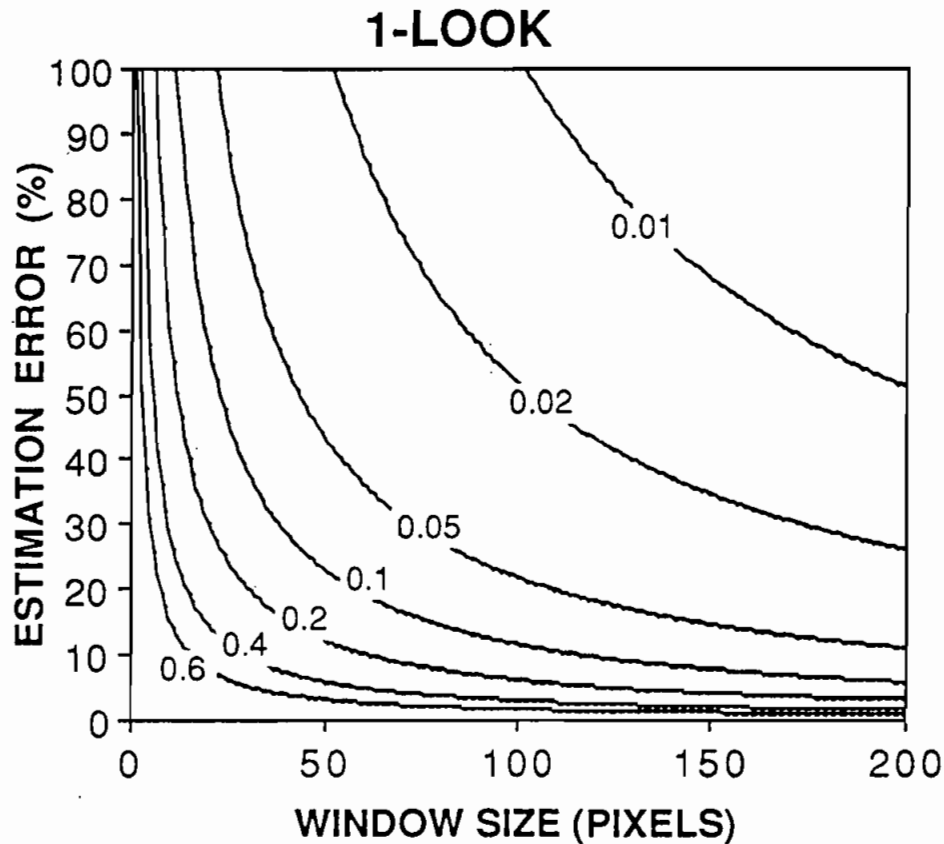
1-LOOK

Figure 2. Estimation error for some values of the image autocovariance coefficient ρ_p for single look SAR data versus the size of a square window.

many conclusions drawn from the observation of airborne SAR data cannot be quickly applied to the prediction of observations from spaceborne SAR data if system noise is not considered.

3.3. *Effect of image speckle*

The approach presented in this paper relies on our capability to correctly estimate the autocovariance coefficient of speckle, i.e., estimate the speckle spectrum. Considerable work on speckle spectrum estimation has already been done in the field of SAR oceanography and estimation of wave spectra (Monaldo and Lyzenga 1986, Beal *et al.* 1983). In Vachon and Raney (1989) the speckle spectrum is estimated by intentionally defocusing the processor. Raney (1983) showed that the speckle spectrum is only a function of system coherence and not a function of scene coherence (i.e., texture) or system focus. Another method is proposed in Cordey and Macklin (1989) using SAR complex data as in that case the autocorrelation function of the complex amplitudes is proportional to the autocovariance coefficient of speckle and does not depend on scene coherence and system focus. Artifacts in the autocovariance coefficient of speckle were mentioned in this paper which have been explained in Rignot and Chellappa (1991) who developed a segmentation technique

for SAR complex data. Ulaby *et al.*(1986) used the image autocovariance coefficient of a patch of calm water with no apparent textural variability to estimate the autocovariance coefficient of speckle. As shown earlier, large window sizes are required for accurate estimation, and water, when present in the imagery, is not always textureless due to surface-wind effects. Therefore, this technique may sometimes not provide reliable estimates of this function.

In our study, we insist that the SAR system is well focused. Clearly, if the SAR system is defocused, the study of intrinsic texture is useless. To estimate ρ_S, we fit a theoretical model with measurements of the actual spatial resolution of the SAR system. In effect, in the presence of a well focused SAR system, ρ_S is equal to ρ_h the autocorrelation coefficient of the SAR system incoherent impulse response. It can be shown (e.g., Barber 1985) that the SAR impulse response function that results from the SAR correlation process is the Fourier transform of the synthetic aperture of the SAR instrument. In general, this aperture is a rectangular window, and ρ_h is a two-dimensional sinc function (with $\text{sinc}(x) = (\sin(\pi x))/(\pi x)$). Yet, additional processing is usually performed to reduce the amplitude of the side lobes of the impulse response for enhancement of data quality. The operation may be done both in range
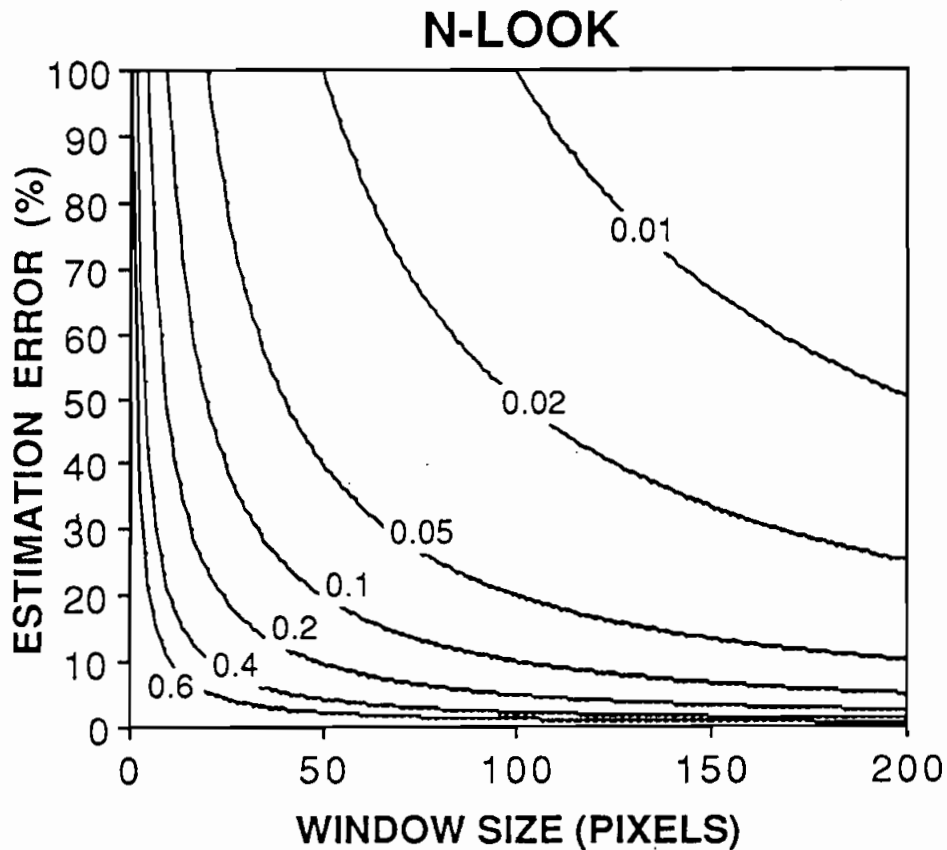

Figure 3.   Estimation error for some values of the image autocovariance coefficient ρ_P for infinite-look SAR data versus the size of a square window.

and azimuth, sometimes using different filters. The actual SAR system impulse response is therefore proportional to the Fourier transform of the weighted synthetic aperture. Similarly, during the selection (usually in the frequency domain) of independent samples used to generate multi-look intensity imagery, various window-ing functions (or pass-band filters) are used that produce an impulse response equal to the Fourier transform of the weighted aperture. In the case of the NASA/JPL DC-8 SAR the synthetic aperture can be modelled as a rectangular window with amplitude weighting using a Hamming filter in range and a Kaiser filter in azimuth. Multi-look filtering (non-coherent summation of samples in the time domain) uses simple sinc filters. The corresponding analytical model of the system coherent impulse response is given in appendix C. The model only depends on the spatial resolution of the data in range and azimuth. The values used for analysis of sea-ice data are based on measurements of the mean resolution of the SAR instrument from corner reflectors of known backscatter characteristics (Freeman 1990). Again, the accuracy of the resolution estimates affects the quality of the model. Typically, the range resolution R_r of the NASA/JPL airborne SAR is known with 10 per cent accuracy which results in a 10 per cent error for ρ_h. The same observation applies to the determination of the equivalent number of looks. Experimentally, in the case of sea-ice SAR data, the contribution of this error was found to be of second order compared to the observed variability of the textural measurements across frequency and across different sea-ice types.

4. Analysis of spatial statistics in sea-ice SAR data

Three-frequency polarimetric sea-ice SAR data were acquired by the NASA/JPL aircraft SAR during the March 1988 Alaska campaign over the Beaufort and Chuckchi seas. The airborne instrument operates at C-, L-, and P-bands (5·656 cm, 23·98 cm, and 68·13 cm wavelengths) simultaneously, and obtains fully polarimetric information by transmitting and receiving a combination of linear polarizations: HH, HV, VH, and VV, where, for example, HV means H-polarization is transmitted and V-polarization is received by the antenna (Held *et al.* 1988). Three scenes from the Beaufort sea were selected to illustrate the technique of analysis of spatial statistics. The images are four-look intensity data where multi-looking was per-formed in azimuth, i.e., not reducing spatial resolution in range. The equivalent number of looks, computed using (5), is 3·1, 3·4 and 3·5 at C-, L-, and P-band frequencies respectively. Spatial resolutions at those frequencies are respectively 11·1 m, 10·7 m and 11·2 m in slant-range and 18·0 m, 16·0 m, 15·6 m in azimuth. Pixel spacing of the digitized images is 6·66 m in slant-range and 12·1 m in azimuth at all three frequencies.

Five different sea-ice types were identified by visual inspection of the data. In decreasing order of radar backscatter cross-section, they are: (1) multi-year ice (MY), which is old ice that survived one or more summer melts, typically several metres thick and of low salinity; (2) first year rough ice (FYR), less than a metre thick, with a lot of ridging and a rough surface; (3) first year smooth ice (FYS), about one meter thick with a smooth surface; (4) frozen lead ice (FL), newly formed ice, a few centimetres thick; and (5) open water. A three-frequency colour overlay of one of the selected images is shown in figure 4. P-band is coded in red, L-band in green, and C-band in blue. The saturation of each colour is proportional to the intensity of the signal at that frequency and the average intensities are set to the middle of the display dynamic range. Figure 5 shows the intensity images obtained
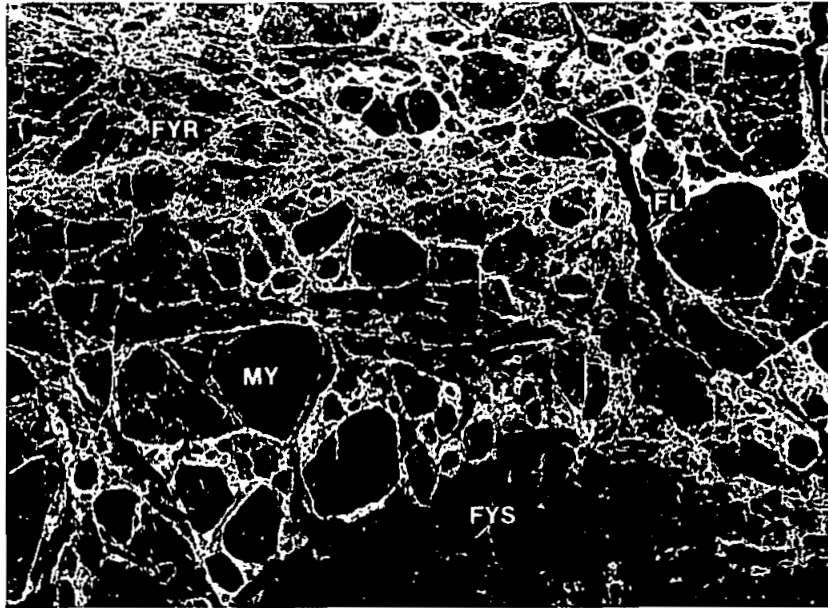
Figure 4.   Colour overlay of multi-frequency SAR data of sea-ice acquired by the NASA/
JPL aircraft SAR at *P*- (Red), *L*- (Green) and *C*- (Blue) band frequency. The image is
1024 pixels by 750 pixels in size. The radar moved from left to right and the
illumination direction is from the top. The letterings on top of the colour overlay
indicate the different sea-ice types identified in the scene. (MY) is multi-year ice; (FYR)
is first year rough sea-ice; (FYS) is the first year smooth sea-ice; and (FL) is frozen lead
ice.

at those three frequencies for different polarization configurations of the SAR
antenna, respectively HH-polarization, VV-polarization, and HV-polarization. The
image is 1024 pixels in azimuth (left to right in the figure) and 750 pixels in range
(top to bottom in the figure). The letterings on top of the colour overlay indicate the
different sea-ice types that have been identified in the scene. Multi-year ice (MY)
patches show a characteristic much brighter return than first year ice at *C*-band
(blue) at this time of the year, and correspond to more rounded geometrical shapes.
Deformed first year ice of different roughnesses and thicknesses is also present in the
imagery (FYR and FYS). Pressure ridges are clearly visible in first year ice as bright
linear features (yellow linear features in figure 5), especially at *L*- and *P*-bands. At
those latitudes and during the winter season, open water is difficult to observe and
depending on conditions only appears in open leads for a few hours before it freezes.
Water was only positively identified in one of our SAR images based on correlative
passive microwave observations and visual inspection of the data.

Several sample windows were selected within the imagery with a number of
elements varying from 325 (open leads) to 3200 pixels (multi-year ice floes). Two
textural characteristics were computed for each window: the standard deviation of
texture σ_T using (3), and the autocovariance area of texture in range using (7) and
defined as

$$A_T = \int_0^2 \rho_T(p, 0)dp \tag{9}$$

The integrated area A_T was found to be a better discriminant than the autocovariance length $\rho_T(1)$ since the correlation length tends to be noisier than the integrated measure. The integration is limited to two pixels because of the limited accuracy in ρ_P for larger displacements (see above). A_T varies between 0 ($\rho_T=0$) and 2 ($\rho_T=1$).
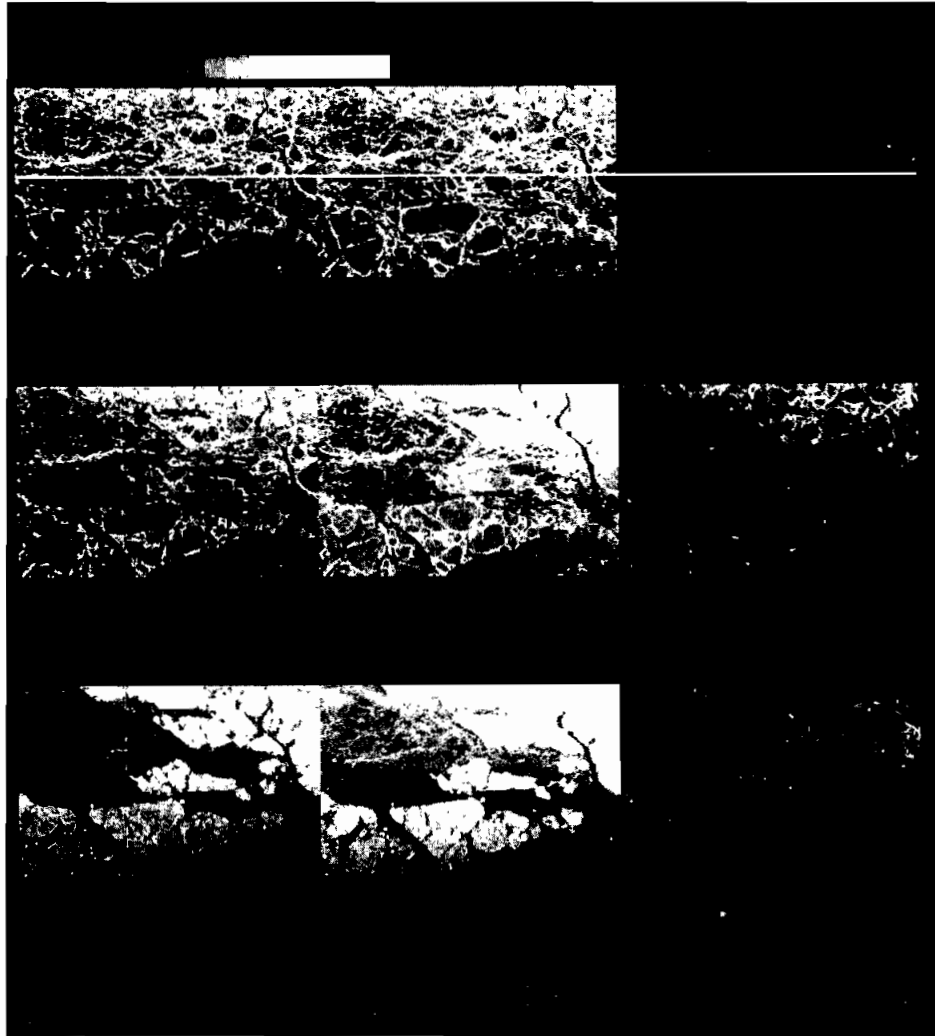

Figure 5. Multi-frequency and multi-polarization SAR data of sea-ice acquired by the NASA/JPL aircraft SAR at *P-* (top), *L-* (middle), and *C-* (bottom) band frequencies. From left to right, amplitude data display obtained using an HH-polarization, a VV-polarization, and an HV-polarization (also see bottom right corner of picture for reference). The transverse white line at *P*-band corresponds to a processing artefact. In each image, the radar moved from left to right and the illumination direction is from the top.
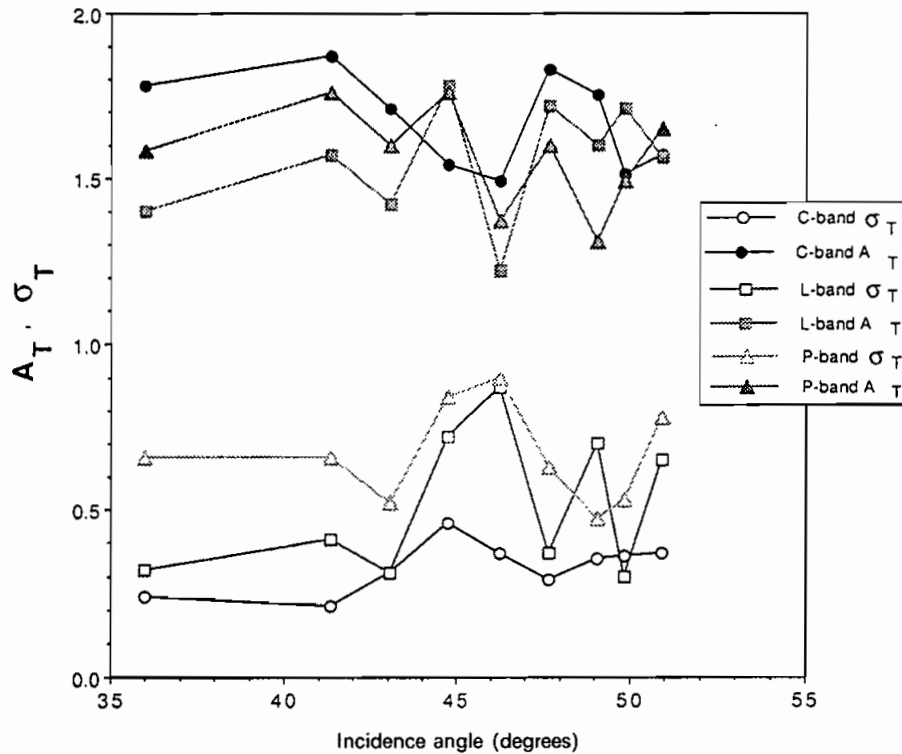
Figure 6. Standard deviation of texture (σ_T) and autocovariance area of texture (A_T) versus the incidence angle for multiyear sea-ice at P-, L- and C-band frequencies and VV-polarization.

The first case corresponds to a textured area where the data is highly uncorrelated, whereas the second case indicates a smooth homogeneous surface with little backscatter variation.

Textural features extracted in azimuth were found to be similar to those obtained in range. Since spatial resolution is more stable in range than in azimuth and of comparable order of magnitude, only the results obtained in slant-range are considered in the discussion.

The effect of incidence angle on the textural measurements was first examined using multi-year ice and first year smooth ice as they were the only sea-ice types systematically present across the entire swath in our data. The results shown in figure 6 indicate that the variability of these measurements with the incidence angle (between 35° and 55°) is insignificant compared to the observed within-class variability of the measurements.

Plots of A_T vs σ_T for the different sea-ice types at various frequencies and polarizations are shown in figures 7 and 8. The limiting case, $A_T \approx 0 \cdot 85$ which corresponds to $\rho_P \approx \rho_S$, is never reached indicating that only a broadening of the image auto-covariance coefficient due to texture is observed in the data set.

The results plotted in figure 7 show little variability of the textural characteristics between HH- and VV-polarizations at L-band. The same observation can be made

at *P*- and *C*-bands (not shown here). Therefore, the spatial statistics seems to be similar across polarization. Only frozen lead ice shows some textural variability across polarization. A possible explanation is that the observed areas are not locally homogeneous and are composed of a mixture distribution of various sea-ice types (ridges in formation, smooth areas, rough areas, etc.) that have different backscatter
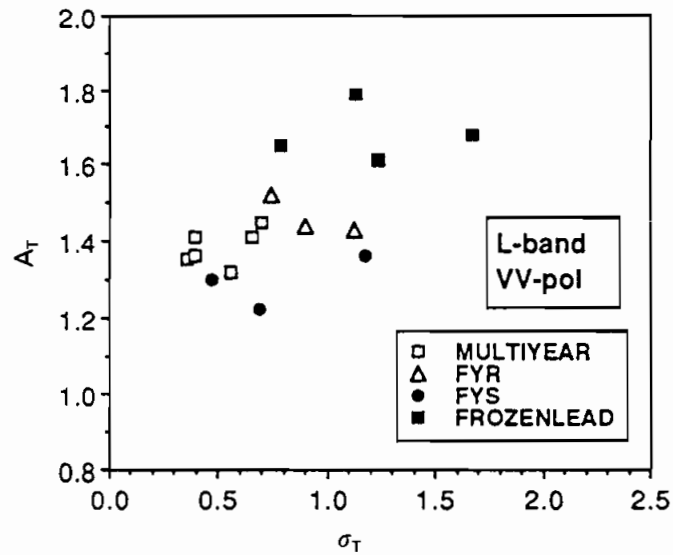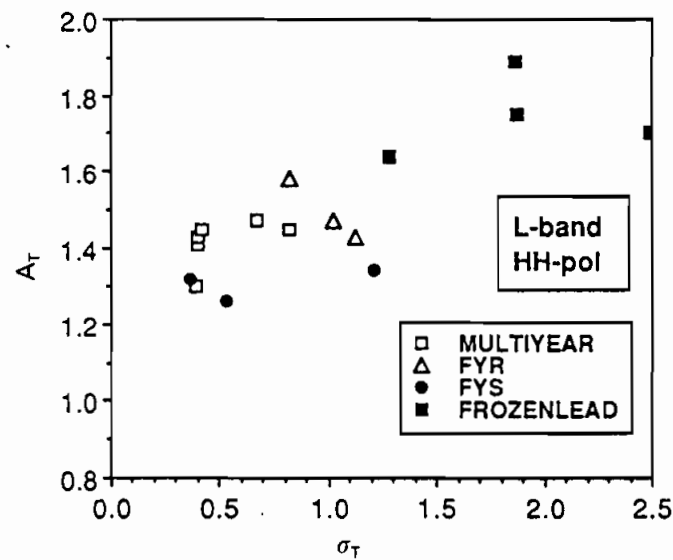
Figure 7. Autocovariance area of texture (A_T) versus the standard deviation of texture (σ_T) at *L*-band frequency for multi-year sea-ice (MULTIYEAR), first year rough (FYR), first year smooth (FYS) and frozen lead (FROZENLEAD). (*a*) VV-polarization; (*b*) HH-polarization.
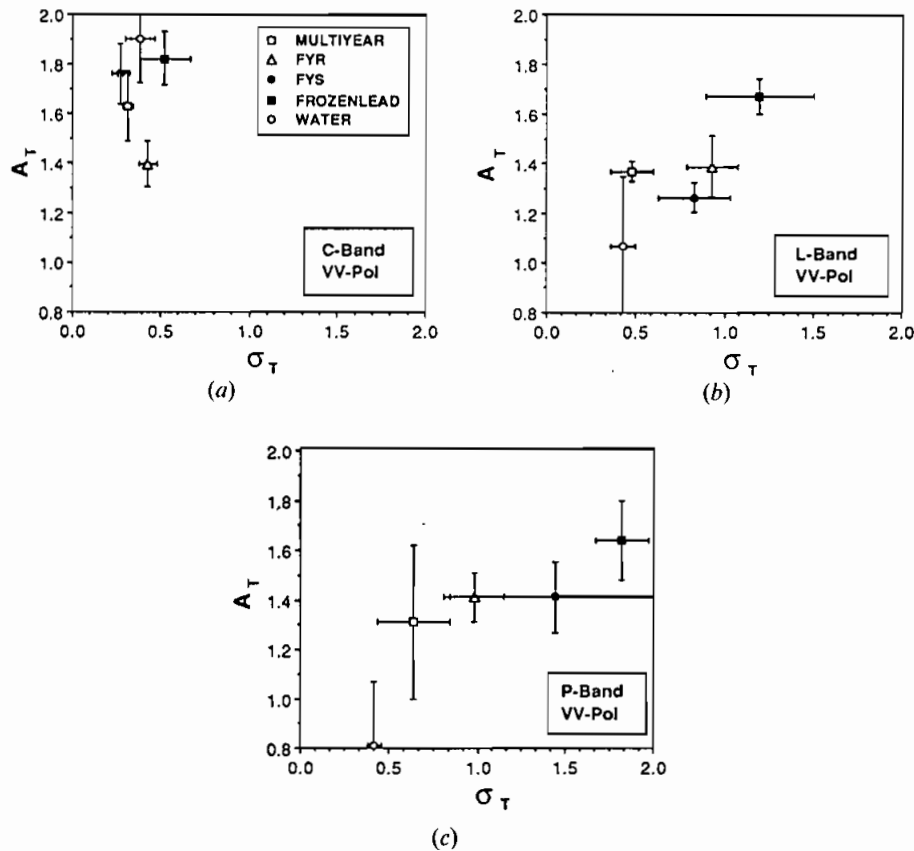
Figure 8. Autocovariance area of texture (A_T) versus the standard deviation of texture (σ_T) for multi-year sea-ice (MULTIYEAR), first year rough (FYR), first year smooth (FYS), frozen lead (FROZENLEAD) and open water (WATER); at VV-polarization and (a) C-band frequency; (b) L-band frequency; and (c) P-band frequency.

characteristics and polarization behaviour, thereby introducing a spatial variability of the signal that is polarization dependent.

Figure 8 shows the average results obtained at VV-polarization and L-, P- and C-bands. Error bars represent the standard deviation of each measurement. At C-band (figure 8 (a)) σ_T is relatively small (about 0·3) and A_T is large. Both features indicate a small random modulation of the signal and rather spatially homogeneous backscatter characteristics. The data set does not suggest texture to be a good discriminant at this frequency. At L-band (figure 8 (b)), texture is more pronounced as σ_T is higher and less correlated as A_T is lower. The trend continues at P-band (figure 8 (c)), a longer wavelength, indicating that σ_T consistently increases and A_T decreases with increasing wavelength. A possible explanation of these observations is that as the wavelength increases and the radar penetrates deeper into the ice the spatial distribution of backscatter cross-section becomes less homogeneous. This varying degree of homogeneity may also be related to the size of the resolution cell, a fact pointed out by Yueh *et al.* (1989) in their study of the first order statistical characteristics of multi-frequency forestry data. In the NASA/JPL aircraft SAR

data the size of the resolution cell is kept nearly constant (between 10·7 and 11·2 m) across frequency. Hence, one resolution cell is about 120 wavelengths wide at *C*-band, 30 wavelengths at *L*-band, and 10 wavelengths at *P*-band. As the number of scattering elements per resolution cell is typically proportional to the number of wavelengths per resolution cell, any variability in the number of scatterers per resolution cell will have a more pronounced effect (i.e., fluctuations in the observed return) on the signal at longer wavelengths than at smaller wavelengths. This effect correlates well with the observed textural measurements.

Textural measurements vary differently with various sea-ice types. Open water has a σ_T which remains fairly constant across frequency, indicating a smooth surface. However, A_T drops unexpectedly from almost 2 at *C*-band (smooth surface) to 0·8 at *P*-band. We do not have an explanation for this behaviour and further investigation is required. On the other hand, the correlation of texture remains constant in frozen leads and first year rough. A possible explanation is the presence of pressure ridges in the ice. The spatial distribution of these ridges does not vary with frequency and hence the correlation length of the signal tends to remain nearly constant.

Multi-year ice is consistently less textured than first year ice as σ_T is smaller. The textural signature of open water is also significantly different from that of first year ice which indicates that texture may be a useful discriminant for single polarization, single frequency SAR data as it is difficult to separate newly formed ice from open water using tonal information alone. At *C*-band, the differences in signatures are not statistically significant, but at *L*- and *P*-bands separability of the measurements is more clear. Note that σ_T alone would not separate these ice types and second order statistics (A_T) are important.

5. Conclusions

A statistical approach to the analysis of spatial statistics in polarimetric multi-frequency SAR data was presented. This approach quantifies the random spatial variability of natural targets by measuring the characteristics of its first and second order spatial statistics after the variability due to image speckle and system noise has been removed. This approach was illustrated using sea-ice imagery acquired by the NASA/JPL aircraft SAR.

Spatial statistics in sea-ice SAR imagery, based on the extracted statistics, reveal that a textural modulation of the signal can be detected and is more apparent at longer wavelengths (23·98 cm to 66·8 cm) than at shorter wavelengths (5·6 cm) and the statistics do not vary significantly with the polarization configuration of the radar antenna and the incidence angle. Good discrimination between sea-ice types that are not well separated using tonal information alone was observed in some cases, especially at longer wavelengths, showing that spatial statistics contain useful discriminative information about the scattering characteristics of sea-ice. In order to verify these measurements and relate the SAR observation to ice scattering physics, *in-situ* sea-ice experiments need to systematically include observations and measurements of the spatial variability of the backscatter characteristics of various ice-floes. As multi-resolution SAR data of sea-ice were not available the influence of spatial resolution on spatial satistics could not be quantified. In the case multi-year ice, finer resolution would be especially interesting since it would reveal the influence of melt ponds on the spatial statistics.

Appendix A. Estimation error of the image variance-to-mean square ratio

If σ and μ denote, respectively, the estimate of the image standard deviation and the estimate of the image mean power, the variance of the estimate of their ratio is given by Kendall and Stuart (1963) as, for a sample of size n (first order),

$$\text{Var}\left(\frac{\sigma}{\mu}\right) = \left[\frac{\langle\sigma\rangle}{\langle\mu\rangle}\right]^2 \left[\frac{\text{Var}(\sigma)}{\langle\sigma\rangle^2} + \frac{\text{Var}(\mu)}{\langle\mu\rangle^2} - 2\frac{\text{Cov}(\sigma,\mu)}{\langle\sigma\rangle\langle\mu\rangle}\right] \tag{10}$$

where $\text{Cov}(x,y)$ is the covariance of x and y, and $\text{Var}(x)$ the variance of x, and μ_i the ith order moment of the power. Computation of these moments using a Gamma-distribution of the power leads to

$$\text{Var}\left(\frac{\sigma}{\mu}\right) \approx \frac{(N+1)}{2N^2 n} \tag{11}$$

$$\text{Var}(V_{mr}) \approx \frac{2(N+1)}{N^3 n} \tag{12}$$

where N is the equivalent number of looks of the SAR data.

Appendix B. Estimation error of the image autocovariance coefficient

If ρ_P denotes the estimate of the image autocovariance coefficient, its variance is given by Kendall and Stuart (1963) as

$$\text{Var}(\rho_P) = \frac{\rho^2}{n}\left[\frac{\mu_{22}}{\mu_{11}^2} + \frac{1}{4}\left\{\frac{\mu_{40}}{\mu_{20}^2} + \frac{\mu_{04}}{\mu_{02}^2} + 2\frac{\mu_{22}}{\mu_{20}\mu_{02}}\right\} - \left\{\frac{\mu_{31}}{\mu_{11}\mu_{20}} + \frac{\mu_{13}}{\mu_{11}\mu_{02}}\right\}\right] \tag{13}$$

where ρ is the true value of the autocovariance coefficient (i.e., $\rho = \mu_{11}/\sqrt{(\mu_{20}\mu_{20})}$), and μ_{ij} the ith and jth order moment of the reduced power (i.e., $\mu_{ij} = \langle[P_1 - \mu_{P1}]^i\rangle\langle[P_2 - \mu_{P2}]^j\rangle$). We have (Goodman 1975)

$$\langle P_1^i P_2^j \rangle = \mu_P^{i+j} i! j! \,_2F_1(-i, -j, 1, \rho_P) \tag{14}$$

where $_2F_1$ is a Gaussian hypergeometric function, leading to

$$\text{Var}(\rho_P) = \frac{1}{n}[1 - \rho]^2[1 + 6\rho + 2\rho^2]. \tag{15}$$

For a Gaussian distribution of the power about its mean value, the variance is (Kendall and Stuart 1963)

$$\text{Var}(\rho_P) = \frac{1}{n}[1 - \rho^2]^2. \tag{16}$$

Appendix C. Analytical model of the SAR impulse response function

Aperture weighting in range uses a Hamming window, and multi-looking is done in azimuth using sinc filters. The resulting impulse response for small squint angles is

$$h(m, n) = h_R(m)h_Z(n) \tag{17}$$

with

$$h_R(m) = \gamma_1 \operatorname{sinc}\left(\pi m \frac{s_R}{R_R}\right) + \gamma_2\left(\operatorname{sinc}\left(\pi m \frac{s_R}{R_R} + \pi\right) + \operatorname{sinc}\left(\pi m \frac{s_R}{R_R} - \pi\right)\right)$$

$$h_Z(n) = \operatorname{sinc}\left(\pi n \frac{s_Z}{R_Z}\right) \tag{18}$$

where s_R and R_R are respectively the sample spacing and the spatial resolution in slant-range, s_Z and R_Z are the same quantities in azimuth, $\gamma_1 \approx 1\cdot073$, and $\gamma_2 \approx 0\cdot457$.

Appendix D. Textural variability from K-distributions

In the traditional approach for modelling of the distribution function of speckled image data, a random walk model is used (Goodman 1975). In the limit of an infinite number of steps in the random walk, the resulting statistics of the complex amplitude field are circular Gaussian (central limit theorem). However, studies by Jakeman and Pusey (1976) revealed that if the number of steps is itself a random variable, even in the limit of a very large number of scatterers, the resulting statistics are not necessarily Gaussian. As a result, the higher order moments of the data have different predicted values, and comparisons with experimental data indicate that in several cases K-distributions better describe the observed statistics (Jakeman and Pusey 1976, Jakeman 1980, Oliver 1986, Yueh *et al.* 1989).

Jakeman (1980) studied the first order statistics of one of these limit distributions using a negative binomial distribution for the number of random steps

$$P_N = C_N^{N+\alpha-1} \frac{(N/\alpha)^N}{(1 + N/\alpha)^{N+\alpha}} \tag{19}$$

where α is a positive parameter, and N is the mean number of random steps. The V_{mr} ratio of a one-look K-distribution is $(2/\alpha + 1)$. Comparison with (3) indicates that σ_T^2 is equivalent to $1/\alpha$. When α is infinite, the amplitude of the signal is Rayleigh distributed and σ_T is zero, a consistent result. As α goes to zero, the fluctuations in the number of scatterers increase and σ_T increases too.

In Jakeman (1980), the spatial variability in the number of scatterers per resolution cell is viewed as a death and birth process parametrized by a death rate μ, a birth rate λ, and an immigration rate ν. The K-distributed model of the covariance coefficient of the power of the signal is

$$\rho_P(d) = \frac{1 + \dfrac{1}{\alpha}}{V_{mr}} \exp\left[-2\mu d\right]\rho_S(d) + \frac{\exp\left[(\lambda - \mu)d\right]}{\alpha} \tag{20}$$

where d is the displacement in pixels. For comparison, assuming no system noise, (7) can be rewritten as

$$\rho_P(d) = \frac{1 + \dfrac{\rho_T(d)}{\alpha}}{V_{mr}} \rho_S(d) + \frac{\rho_T(d)}{\alpha}. \tag{21}$$

The two expressions are similar but not equivalent. One reason is that Jakeman's model implicitly assumes that texture has a correlation function of exponential type,

whereas our model makes no assumption. Very few studies have been made on correlated K-distributions and to the best of our knowledge an exponential behaviour of ρ_T has not been demonstrated using real SAR data. Further, a model based on K-distribution assumes that the only source of textural variability of the signal is the number of scatterers per resolution cell. Our model does not exclude the influence of other factors and is therefore more appropriate to the characterization of spatial statistics in SAR imagery.

References

BARBER, B. C., 1985, Theory of digital imaging from orbital synthetic aperture radar. *International Journal of Remote Sensing*, **6**, 1009–1057.

BEAL, R. C., TILLEY, D. G., and MONALDO, F. M., 1983, Large- and small-scale spatial evolution of digitally processed ocean wave spectra from Seasat synthetic aperture radar. *Journal of Geophysical Research*, **88**, 1761–1778.

CORDEY, R. A., and MACKLIN, J. T., 1989, Complex SAR imagery and speckle filtering for wave imaging. *I.E.E.E. Transactions on Geoscience and Remote Sensing*, **GE-27**, 666–673.

FREEMAN, A., 1990, An image quality assessment of the NASA/JPL aircraft SAR during Spring 1988, JPL D-7197 (Pasadena, California: NASA's Jet Propulsion Laboratory).

FROST, V. S., STILES, J. A., SHANMUGAN, K. S., and HOLTZMAN, J. C., 1982, A model for radar images and its application to adaptive digital filtering for multiplicative noise. *I.E.E.E. Transactions on Pattern Analysis and Machine Intelligence*, **PAMI-4**, 157–166.

GOODMAN, J. W., 1975, Statistical Properties of Laser Speckle Patterns. In *Laser Speckle and Related Phenomena*, edited by J. C. Dainty (Heidelberg: Springer Verlag), volume 9 of *Topics in Applied Physics*, pp. 9–75.

HARALICK, R. M., SHANMUGAN, M. K., and DINSTEIN, S., 1973, Textural features for image classification. *I.E.E.E. Transactions on System, Man, Cybernetics*, **SMC-3**, 610–621.

HELD, D. N., BROWN, W. E., FREEMAN, A., KLEIN, J. D., ZEBKER, H., SATO, T., MILLER, T., NQUYEN, Q., and LOU, Y., 1988, The NASA/JPL multifrequency, multipolarization airborne SAR system. *Proceedings of IGARSS' 1988 Symposium, Edinburgh, U.K., on 12–16 September 1988* (Paris: European Space Agency), pp. 345–350.

JAKEMAN, E., 1980. On the statistics of K-distributed noise. *Journal of Physics* A, **13**, 31–48.

JAKEMAN, E., and PUSEY, P. N., 1976, A model for non-Rayleigh sea echo. *I.E.E.E. Transactions on Antenna and Propagation*, **AP-24**, 806–814.

KENDALL, M. G., and STUART, A. S., 1963, The Advanced Theory of Statistics, volume I. *Distributed Theory* (New York: Hafner Publishers), chap. 10.

KOUYATE, F., 1984, SAR imagery analysis: Scene statistics and a textural approach to classification. Ph.D. Thesis, University of Kansas, Lawrence.

LAUR, H., 1989, Analyse d'images radar en télédétection: discriminateurs radiométriques et texturaux. Ph.D. Thesis, Université Paul Sabatier de Toulouse, France, No. 403.

LEE, J. S., 1981, Speckle analysis and smoothing of synthetic aperture radar images, *Computer Graphics and Image Processing*, **17**, 24–32.

LYDEN, J. D., BURNS, B., and MAFFET, A. L., 1984, Characterization of sea-ice types using synthetic aperture radar. *I.E.E.E. Transactions on Geoscience and Remote Sensing*, **GE-22**, 431–439.

MADSEN, S., 1986, Speckle Theory: Modeling, analysis, and applications related to synthetic aperture radar data. Ph.D. Thesis, Technical University Denmark Lyngby, LD 62.

MONALDO, F. M., and LYZENGA, D. R., 1986, On the estimation of wave slope and height variance spectra from SAR imagery. *I.E.E.E. Transactions on Geoscience and Remote Sensing*, **GE-24**, 543–551.

OLIVER, C. J., 1986, The interpretation and simulation of clutter textures in coherent images. *Inverse Problems*, **2**, 481–518.

RANEY, R. K., 1983, Transfer functions for partially coherent SAR systems. *I.E.E.E. Transactions on Aerospace and Electronic Systems*, **AES-19**, 740–750.

RIGNOT, E., and CHELLAPPA, R., 1991, Segmentation of synthetic aperture radar complex data. *Journal of Optical Society of America*, A, **8**, 1499–1509.

ULABY, F., KOUYATE, F., BRISCO, B., and LEE WILLIAMS, T. H., 1986, Textural information in SAR images. *I.E.E.E. Transactions on Geoscience and Remote Sensing*, **GE-24**, 235–245.

VACHON, P. W., and RANEY, R. K., 1989, Estimation of the SAR system transfer function through processor defocus. *I.E.E.E. Transactions on Geoscience and Remote Sensing*, **GE-27**, 702–707.

YUEH, S. H., KONG, J. A., JAO, J. K., SHIN, R. T., ZEBKER, H. A., LE TOAN, T., 1989, K-distribution and multifrequency terrain radar Clutter. *Journal of Electromagnetic Waves and Applications*, **3**, 747–768.

ZELENKA, J., 1976, Comparison of continuous and discrete mixed-integrator processors. *Journal of Optical Society America*, A, **66**, 1295–1304.